RSC Advances

PAPER

View Article Online
View Journal | View Issue

Cite this: *RSC Adv.*, 2022, **12**, 5466

Silver cluster doped graphyne (GY) with outstanding non-linear optical properties†

Saba Zahid,[a] Alvina Rasool,[a] Ali Raza Ayub,[a] Khurshid Ayub,[b] Javed Iqbal,*[ac] M. S. Al-Buriahi,[d] Norah Alwadai[e] and H. H. Somaily[fg]

This research study addresses the computational simulations of optical and nonlinear optical (NLO) characteristics of silver (Ag) cluster doped graphyne (**GY**) complexes. By precisely following DFT and TD-DFT hypothetical computations, in-depth characterization of **GY@Ag$_{center}$**, **GY@Ag$_{side}$**, **GY@2Ag$_{perpendicular}$**, **GY@2Ag$_{above}$**, and **GY@3Ag$_{center}$** is accomplished using CAM-B3LYP/LANL2DZ while the CAM-B3LYP/mixed basis set is used for study of **2GY@Ag$_{center}$**, **2GY@Ag$_{side}$**, **2GY@2Ag$_{perpendicular}$**, **2GY@2Ag$_{above}$**, and **2GY@3Ag$_{center}$**. The effects of various graphyne surface based complexes on hyperpolarizabilities, frontier molecular orbitals (FMOs), density of states (DOS), absorption maximum (λ_{max}), binding energy (E_b), dipole moment (μ), electron density distribution map (EDDM), transition density matrix (TDM), electrostatic potential (ESP), vertical ionization energy (E_{VI}) and electrical conductivity (σ) have been investigated. Infrared (IR), non-covalent interaction (NCI) analysis accompanied by isosurface are performed to study the vibrational frequencies and type of interaction. Doping strategies in all complexes impressively reformed charge transfer characteristics such as narrowing band gap (E_g) in the range of 2.58–4.73 eV and enhanced λ_{max} lying in the range of 368–536 nm as compared to pure **GY** with 5.78 eV E_g and 265 nm λ_{max} for (**GY@Ag$_{center}$**–**GY@3Ag$_{center}$**). In the case of (**2GY@Ag$_{center}$**–**2GY@3Ag$_{center}$**), when compared to **2GY** with 5.58 eV E_g and 275 nm absorption, maximum doping techniques have more effectively modified λ_{max} in the region of 400–548 nm and E_g, which is in the order of 2.55–4.62 eV. **GY@3Ag$_{center}$** and **2GY@3Ag$_{center}$** reflected a noteworthy increment in linear polarizability α_O (436.90 au) and (586 au) and the first hyperpolarizability β_O (5048.77 au) and (17 270 au) because of their lowest excitation energy (ΔE) when studied in comparison with **GY** (α_O = 281.54 and β_O = 0.21 au) and **2GY** surface (α_O = 416 and β_O = 0.06 au). Focusing on harmony between the tiny Ag clusters and graphyne surface as well as their influences on NLO properties, graphyne doping using its two-unit cells (**2GY**) is found to be expedient for the development of future nanoscale devices.

Received 5th November 2021
Accepted 20th January 2022

DOI: 10.1039/d1ra08117a

rsc.li/rsc-advances

1. Introduction

With the breakthroughs of the ruby laser in 1960 and the second harmonic generation (SHG) in 1961, Franklin and his associates centralized their study on the non-linear optical (NLO) field, and this field turned into a progressive and distinctive discipline in interdisciplinary research.[1] NLO materials are turning out to be extremely prevalent on account of their probable uses in light emitters,[2] photonics,[3] optical switching[4] and holographic imaging[5] as well as electro-opto modulations.[6] For thirty years, NLO processes were mostly overlooked after being hypothesized in the 1930s. Recent hi-tech implementations encompass luminous materials gyroscopes,[7] frequency mixing, biosensor scanners,[8] SHG, and optical switching.[9] The computation of a substantial amount of data produced from diverse origins demands influential and proficient computers. Optical technology provides various methodologies of expanding information handling capabilities.[10] Increasing computing demands can be executed by NLO materials, for this reason, numerous modern organic and inorganic NLO active materials have been developed.[11]

[a]*Department of Chemistry, University of Agriculture, Faisalabad-38000, Pakistan. E-mail: Javedkhattak79@gmail.com; Javed.iqbal@uaf.edu.pk*

[b]*Department of Chemistry, COMSATS University, Abbottabad Campus, Abbottabad-22060, Pakistan*

[c]*Punjab Bio-energy Institute, University of Agriculture, Faisalabad-38000, Pakistan*

[d]*Department of Physics, Sakarya University, Sakarya, Turkey*

[e]*Department of Physics, College of Science, Princess Nourah bint Abdulrahman University, P.O. Box 84428, Riyadh 11671, Saudi Arabia*

[f]*Research Center for Advanced Materials Science (RCAMS), King Khalid University, P. O. Box 9004, Abha 61413, Saudi Arabia*

[g]*Department of Physics, Faculty of Science, King Khalid University, P. O. Box 9004, Abha, Saudi Arabia*

† Electronic supplementary information (ESI) available: Optimized cartesian coordinates of our studied compounds are also available. See DOI: 10.1039/d1ra08117a

Organic molecules based on NLO materials such as dibenzoboroles,[12] benzimidazoles, and chalcogens have been forefront in designing such materials due to their increased value of NLO coefficient, structural and electrical properties.[13] Because of desirable characteristics like greater thermal stability, facile synthesis, inexpensive, strength, and good transparency, inorganic molecules *i.e.*, phosphides and nitrides based NLO materials with considerable first or second hyperpolarizabilities had gained considerable research interest.[14] Significant variety of ordinary methodologies namely diradical character,[15] donor–acceptor π bridge system,[16] excess electron model,[17] and octupolar molecules[18] have been introduced to acquire ultrarapid high response NLO materials with exceptional hyperpolarizability.

GY,[19] as a novel non-natural carbon allotrope initially suggested by Baughman in 1987 (ref. 20) made up of sp-hybridized (ethynyl units) and sp^2-hybridized (benzene rings) carbon[21] comparable to graphite/graphene (GR), has drawn the interest of researchers owing to its fascinating electrochemical, optoelectronic, and structural characteristics, as well as prospective microelectronic and power storage applications.[22–25] However, as far as we could possibly know the effect of doping of silver (Ag) cluster on the external layer of **GY** has yet to be accounted for. In view of this, the goal of this investigation is to determine the consequences of Ag cluster doping with **GY** on NLO and optoelectronic properties.

In this research project motivated by systematic exploration of graphyne, we performed simulations using one-unit celled graphyne as well as two-unit celled graphyne named as **GY** and **2GY** respectively, five different Ag clusters doped with **GY** surface namely **GY@Ag$_{center}$**, **GY@Ag$_{side}$**, **GY@2Ag$_{perpendicular}$**, **GY@2Ag$_{above}$**, and **GY@3Ag$_{center}$** are studied under model 1, each varying in orientation and number of dopant (Ag) on the surface (**GY**). Additionally, doping of Ag clusters on **2GY** generated five different doped complexes namely **2GY@Ag$_{center}$**, **2GY@Ag$_{side}$**, **2GY@2Ag$_{perpendicular}$**, **2GY@2Ag$_{above}$**, and **2GY@3Ag$_{center}$** which are studied under model 2.

GY@Ag$_{center}$ and **2GY@Ag$_{center}$** possess one Ag atom doped on **GY** and **2GY** at their center. **GY@Ag$_{side}$** and **2GY@Ag$_{side}$** had one Ag atom doped at the sides of their surfaces. **GY@2Ag$_{perpendicular}$**, as well as **2GY@2Ag$_{perpendicular}$** contain two Ag atoms doped in a perpendicular direction in the central cavity of **GY** and **2GY**. **GY@2Ag$_{above}$** and **2GY@2Ag$_{above}$** retain two Ag atoms just above the **GY** as well as **2GY** surface. While **GY@3Ag$_{center}$** and **2GY@3Ag$_{center}$** contain three Ag atoms in the central cavity of **GY** and **2GY**. All of the doped complexes are found to be sufficiently stable. Fig. 1 shows a schematic diagram of model 1 and model 2.

2. Computational details

The Gaussian 09 simulation program[26] has been used to perform all computations for (**GY@Ag$_{center}$**–**2GY@3Ag$_{center}$**) and **GY** as well as **2GY**. Structures of all molecules under category of model 1 are optimized using CAM-B3LYP[27] functional in association with the LANL2DZ basis set. While structures of complexes under the category of model 2 *i.e.* **2GY@Ag$_{center}$**, **2GY@Ag$_{side}$**, **2GY@2Ag$_{perpendicular}$**, **2GY@2Ag$_{above}$**, **2GY@3Ag$_{center}$** and **2GY** are optimized using CAM-B3LYP/mixed basis. In mixed basis set of model 2 molecules, dopant (Ag) is optimized at LANL2DZ and **2GY** surface *via* 6-31G basis set. To validate the type of computed geometries, frequency estimations were also conducted on the coordinates of optimized geometry. The molecular geometry, frontier molecular orbitals (FMOs), together with electrostatic potential (ESP) are extracted from optimized structures. UV-Vis spectral simulations of model 1 and model 2 are performed using time-dependent density functional theory (TD-DFT) along with their respective basis set with CAM-B3LYP functional. IEFPCM[28] is employed to specifically analyse the influence of H_2O and $CHCl_3$ on absorption (λ_{max}) of complexes of model 1 and model 2 respectively. The λ_{max} of researched molecules is processed in gas in addition to solvent phase. The Swizard program[29] has been used to compute spectral values and graphed with Origin 6.0 [22]. Interaction energies (E_{int}) are approximated

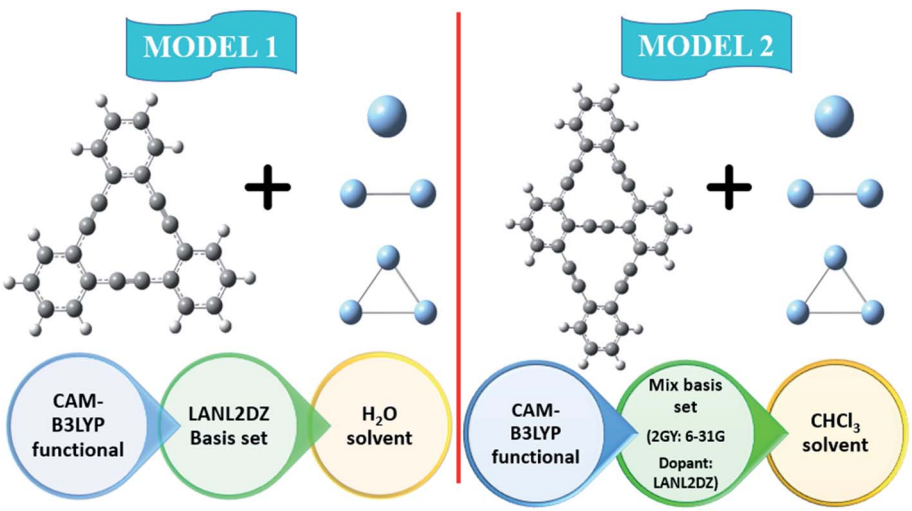

Fig. 1 Schematic diagram of model 1 as well as model 2.

using the following relation[30] to substantiate the thermodynamic stability of our doped surfaces (**GY** and **2GY**).

$$E_{int} = E_{d\_nGY} - (E_{nGY} + E_{n\_Ag}) \quad (1)$$

Here, E_{d_nGY}, E_{nGY} and E_{n_Ag} are energies of doped graphene, pure graphene, and n number of silver (Ag) and graphyne unit cells respectively. Vertical ionization energy (E_{VI}) is also evaluated using eqn (2) (ref. 31) given below

$$E_{VI} = E_{d\_nGY}^{+} - E_{d\_nGY} \quad (2)$$

Here, $E_{d\_nGY}^{+}$ and E_{d_nGY} represent cationic energy of Ag doped surfaces (**GY** and **2GY**) and neutral energy of Ag doped surfaces (**GY** and **2GY**). PyMOlyze 1.1 software[32] has been used to visualize DOS files while Multiwfn 3.7 tool[33] was used to determine electron densities. The same functional is also used electron density difference map (EDDM), dipole moment (μ), and infrared (IR) analysis. Hyperpolarizabilities are the most prevalent indicator of molecule's NLO response.

Through CAM-B3LYP/LANL2DZ basis set and CAM-B3LYP/ mixed basis set, the α_{iso} and α_{aniso} (linear static polarizability), and β_{static} (first hyperpolarizability) are computationally estimated using expressions[9,34] given below

$$\alpha_0 = \frac{1}{3}(\alpha_{xx} + \alpha_{yy} + \alpha_{zz}) \quad (3)$$

$$\beta_0 = (\beta_x^2 + \beta_y^2 + \beta_z^2) \quad (4)$$

In equation, $\beta_x = \beta_{xxx} + \beta_{xxy} + \beta_{xxz}$, $\beta_y = \beta_{yyy} + \beta_{yzz} + \beta_{yxx}$, and $\beta_z = \beta_{zzz} + \beta_{zxx} + \beta_{zyy}$.

3. Results and discussion

3.1 Geometry optimization

Optoelectronic characteristics are greatly influenced by molecular geometry. In model 1, CAM-B3LYP/LANL2DZ functional is used to optimize the pure **GY** as well as newly dopped molecules (**GY@Ag$_{center}$**–**GY@3Ag$_{center}$**). Model 2 employs CAM-B3LYP/ mixed basis set to optimize the pure **2GY** as well as newly dopped systems (**2GY@Ag$_{center}$**–**2GY@3Ag$_{center}$**). The front and side views of optimized frameworks of all molecules of model 1 and model 2 are shown in Fig. 2.

3.2 Photophysical properties

It's crucial to look at UV-visible spectra while researching electronic excitations and charge transfer. The absorption profile of model 1 having pure **GY** and doped complexes (**GY@Ag$_{center}$**–**GY@3Ag$_{center}$**) is computed with CAM-B3LYP/LANL2DZ functional in the gaseous phase and H_2O solvent while that of model 2 *via* CAM-B3LYP/mixed basis set in gaseous phase and $CHCl_3$ solvent. The absorption profile of model 1 along with model 2 illustrates that all newly doped complexes are associated with higher wavelength than the **GY** surface in the gaseous phase as expressed in Fig. 3. Fig. 4 revealed that the employment of solvent as well as shifting toward higher unit cells of **GY** is due to stabilization of π-electrons.[35] **GY@3Ag$_{center}$** has explored the highest λ_{max} in the gaseous phase (522 nm) together with H_2O phase (536 nm) amongst all molecules of model 1 due to the presence of three atoms of Ag on the **GY** surface. The λ_{max} of all complexes in solvent phase is increasing as **GY**< **GY@Ag$_{side}$** < **GY@Ag$_{center}$** < **GY@2Ag$_{above}$** < **GY@2Ag$_{perpendicular}$** < **GY@3Ag$_{center}$**. Likewise, the highest λ_{max} in the gaseous phase (538 nm) as well as in the solvent phase (548 nm) among (**2GY**–**2GY@3Ag$_{center}$**) complexes has been examined by **2GY@3Ag$_{center}$**.

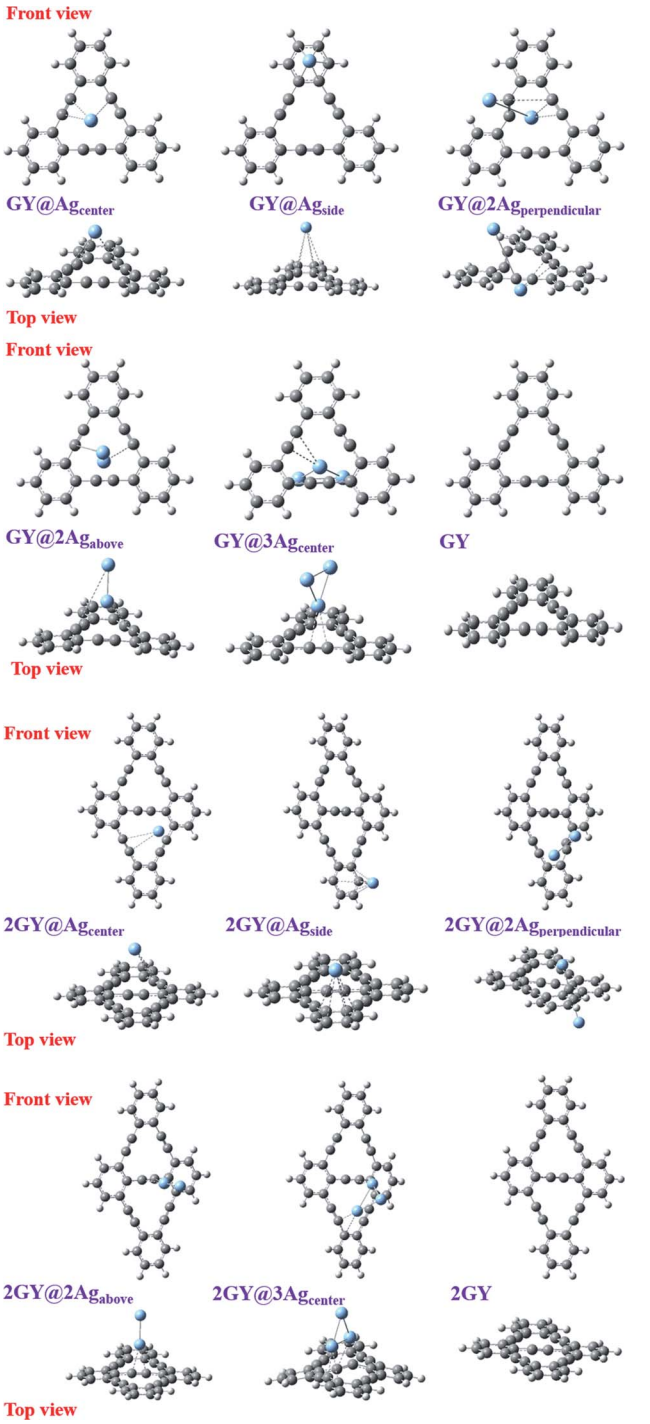

Fig. 2 Framework of all optimized structures from front and top views.

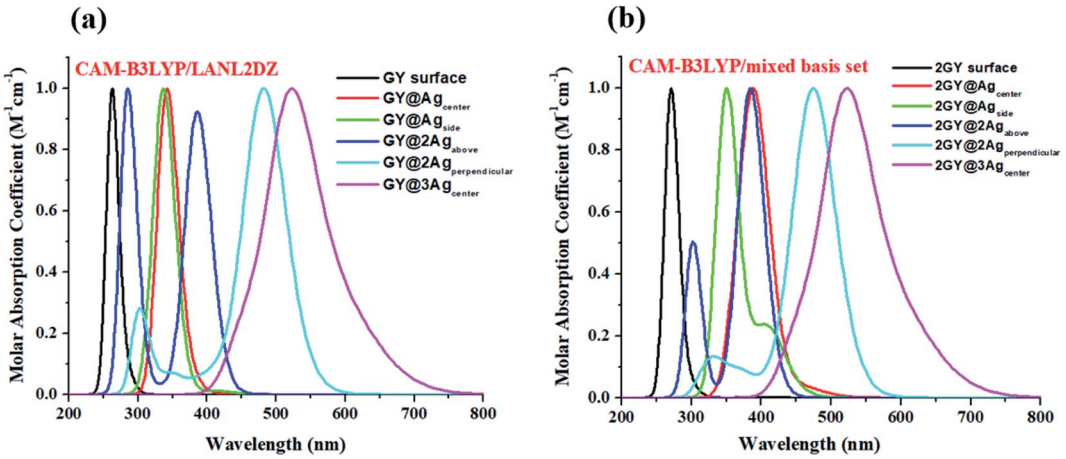

Fig. 3 UV-visible absorption graphs in gaseous phase of molecular complexes of (a) model 1 and (b) model 2.

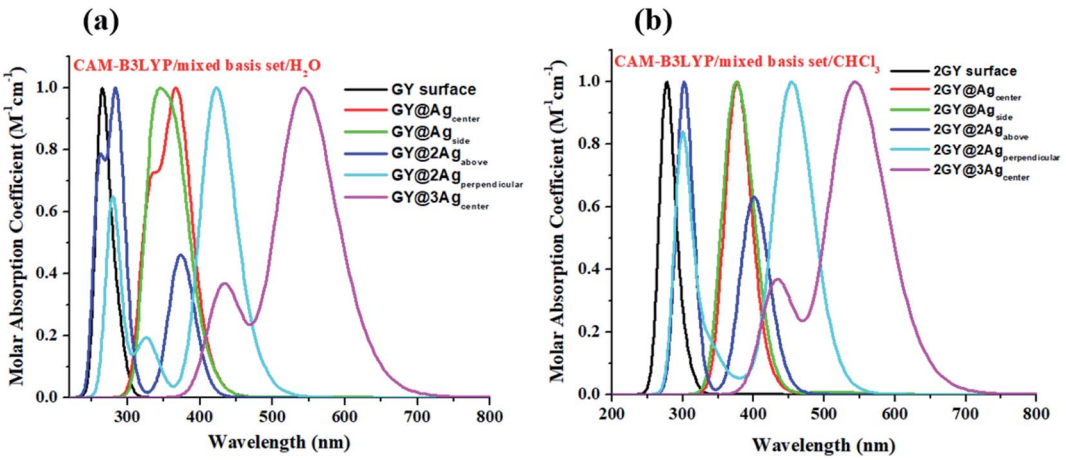

Fig. 4 UV-visible absorption graphs in solvent phase of molecular complexes of (a) model 1 and (b) model 2.

The band gap (E_g) together with λ_{max} are in intense correlation. Lower E_g makes the electronic excitation feasible. Narrow E_g is often interlinked to low kinetic stability since it is energetically preferable to remove electrons from low energy HOMO or add electrons to high energy LUMO resulting in the formation of activated complexes. However, because of lower E_g, these doped systems can be regarded as n-type semiconductors.[21] These doped complexes have been regarded as novel members

Table 1 Computed λ_{max}, excitation energy (E_{opt}), highest oscillator strength f_{OC}, major molecular transitions of molecular systems of model 1 (GY–GY@3Agcenter) and model 2 (2GY–2GY@3Agcenter) in the gaseous phase

Molecules	λ_{max} (nm)	E_{opt} (eV)	f_{OC}	Major molecular transitions (HOMO = H, LUMO = L)
GY	262	4.72	1.1619	H → L (69%)
GY@Ag$_{center}$	342	3.62	0.0991	H → L (72%)
GY@Ag$_{side}$	343	3.62	0.1043	H → L (90%)
GY@2Ag$_{perpendicular}$	483	2.97	0.3980	H → L (66%)
GY@2Ag$_{above}$	386	3.41	0.5394	H → L (70%)
GY@3Ag$_{center}$	522	2.37	0.0923	H → L (100%)
2GY	269	4.60	2.2631	H → L (66%)
2GY@Ag$_{center}$	393	3.15	0.0025	H → L (52%)
2GY@Ag$_{side}$	410	2.97	0.0031	H → L (58%)
2GY@2Ag$_{perpendicular}$	475	2.60	0.4104	H → L (67%)
2GY@2Ag$_{above}$	385	3.22	0.5690	H → L (70%)
2GY@3Ag$_{center}$	538	2.36	0.0923	H → L (76%)

Table 2 Computed λ_{max}, excitation energy (E_{opt}), highest oscillator strength f_{OC}, major molecular transitions of molecular systems of model 1 (GY–GY@3Agcenter) and model 2 (2GY– 2GY@3Agcenter) in the solvent phase

Molecules	λ_{max} (nm)	E_{opt} (eV)	*f*OC	Major molecular transitions (HOMO = H, LUMO = L)
GY	265	4.68	1.1767	H → L (69%)
GY@Ag$_{center}$	368	3.37	0.1407	H → L (93%)
GY@Ag$_{side}$	362	3.43	0.1773	H → L (95%)
GY@2Ag$_{perpendicular}$	421	2.94	0.4358	H → L (67%)
GY@2Ag$_{above}$	373	3.32	0.6140	H → L (70%)
GY@3Ag$_{center}$	536	2.31	0.1283	H → L (100%)
2GY	275	4.51	2.5857	H → L (66%)
2GY@Ag$_{center}$	400	3.29	0.1376	H → L (82%)
2GY@Ag$_{side}$	400	3.30	0.0009	H → L (63%)
2GY@2Ag$_{perpendicular}$	465	2.75	0.4577	H → L (76%)
2GY@2Ag$_{above}$	410	3.09	0.6636	H → L (70%)
2GY@3Ag$_{center}$	548	2.31	0.1283	H → L (93%)

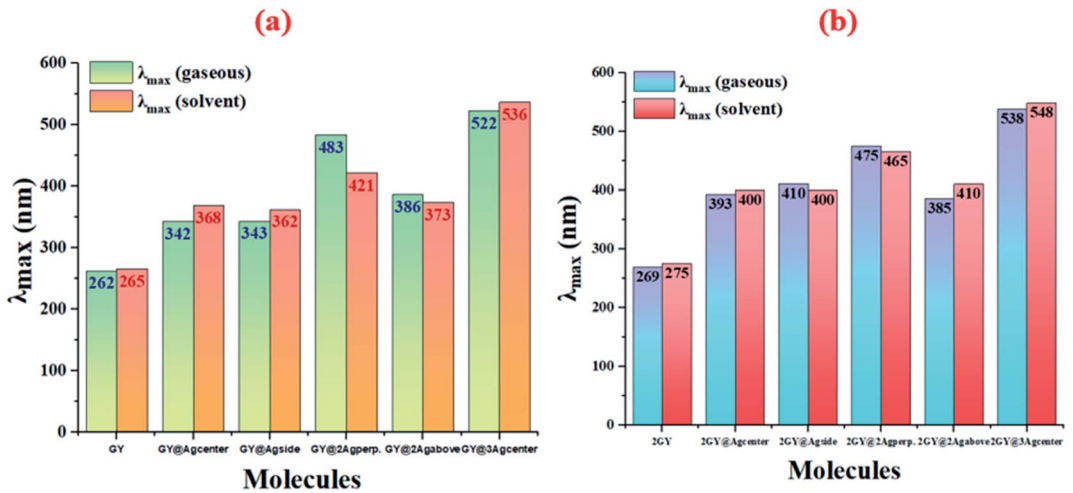

Fig. 5 Graphical representation of comparison of absorption maximum (λ_{max}) in gaseous phase and solvent phase of (a) model 1 molecules (b) model 2 molecules.

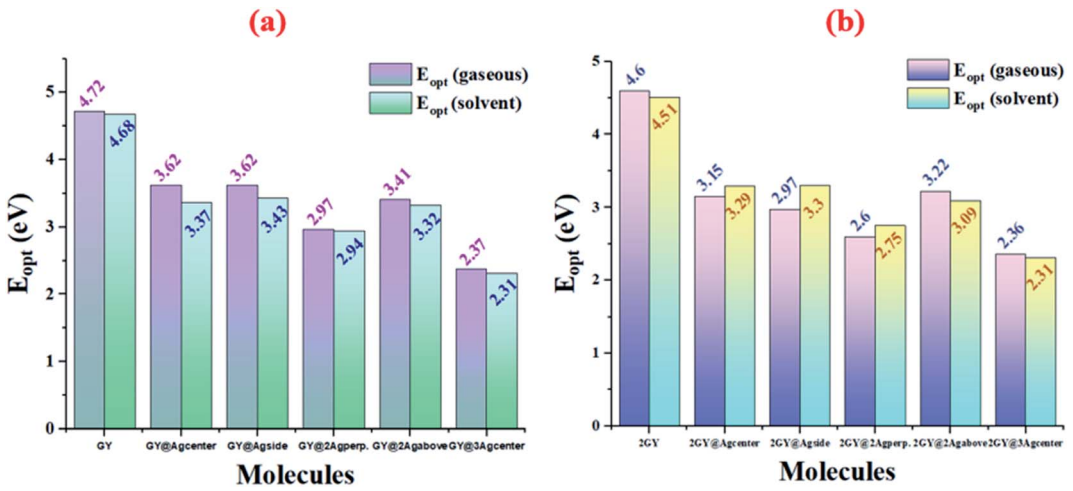

Fig. 6 Graphical representation of comparison of excitation energy (E_{opt}) in gaseous phase and solvent phase of (a) model 1 molecules (b) model 2 molecules.

Table 3 HOMO and LUMO energies, E_g, vertical ionization energies (E_{VI}), interaction energies (E_{int}) and binding energy (E_b) of all investigated molecular complexes

Molecules	HOMO (eV)	LUMO (eV)	E_g (eV)	E_{VI} (eV)	E_{int} (kcal mol^{-1})	E_b (eV)
GY	−6.85	−1.07	5.78	6.85	—	1.1
GY@Ag$_{center}$	−5.36	−1.18	4.18	5.36	−1.69	0.81
GY@Ag$_{side}$	−5.87	−1.14	4.73	5.87	−0.97	1.3
GY@2Ag$_{perpendicular}$	−5.97	−1.38	4.59	5.97	14.69	1.65
GY@2Ag$_{above}$	−5.56	−1.34	4.22	5.56	−6.18	0.9
GY@3Ag$_{center}$	−4.03	−1.45	2.58	4.03	−9.44	0.27
2GY	−6.86	−1.27	5.58	6.86	—	1.07
2GY@Ag$_{center}$	−5.38	−1.35	4.03	5.38	−1.57	0.74
2GY@Ag$_{side}$	−5.90	−1.31	4.58	5.90	−0.93	1.28
2GY@2Ag$_{perpendicular}$	−6.05	−1.42	4.62	6.05	14.41	1.87
2GY@2Ag$_{above}$	−5.38	−1.35	4.03	5.38	−5.95	0.94
2GY@3Ag$_{center}$	−4.00	−1.45	2.55	4.00	−10.44	0.24

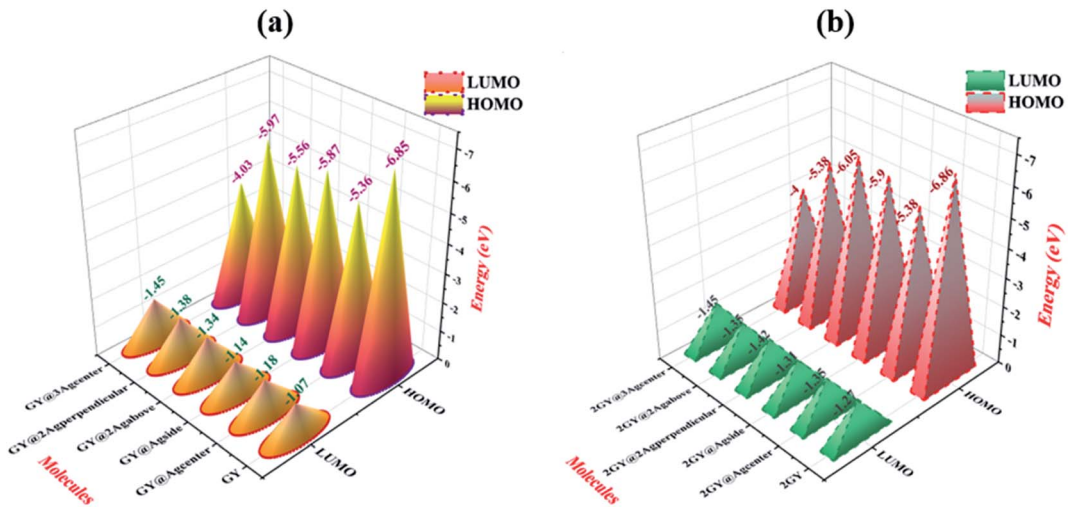

Fig. 7 Graphical description of processed HOMO LUMO orbitals of (a) **GY** and (**GY@Ag$_{center}$**–**GY@3Ag$_{center}$**) and (b) **2GY** and (**2GY@Ag$_{center}$**–**2GY@3Ag$_{center}$**).

of NLO materials. Values of λ_{max}, excitation energy (E_{opt}) and oscillator strength (f_{OC}) in both phases are summarized in Tables 1 as well as 2 respectively.

Results of tables confirmed that the employment of solvent has redshifted the λ_{max} of molecules of both models. Absorption (λ_{max}) values of studied systems such as **GY**, **GY@Ag$_{center}$**,

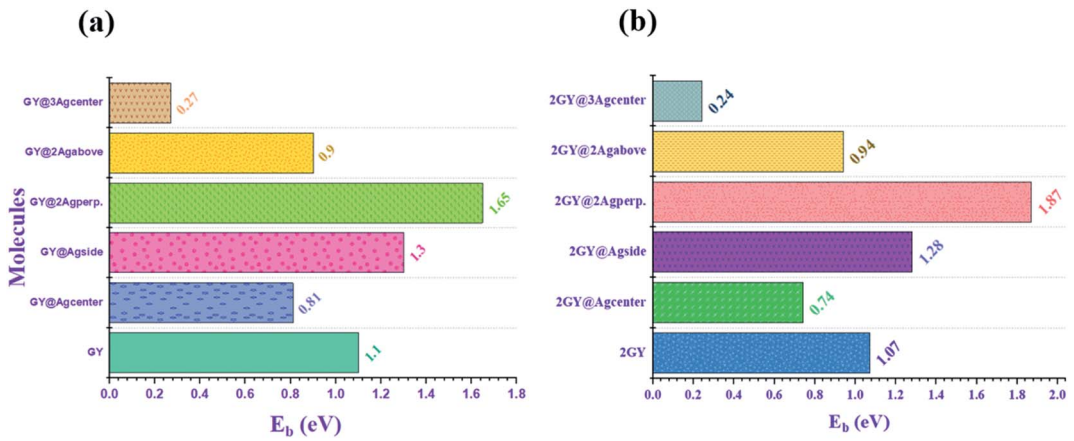

Fig. 8 Graphical illustration of computed binding energy (E_b) of (a) **GY** and (**GY@Ag$_{center}$**–**GY@3Ag$_{center}$**) and (b) **2GY** and (**2GY@Ag$_{center}$**–**2GY@3Ag$_{center}$**).

GY@Ag$_{side}$, **GY@3Ag$_{center}$**, **2GY**, **GY@Ag$_{center}$**, **GY@3Ag$_{above}$**, and **GY@3Ag$_{center}$** are shifted to higher values in solvent. Like, λ_{max} of pure surface **GY** and **2GY** is 262 and 269 nm in gaseous phase; 265 and 275 nm in H_2O owing to the stabilization of delocalized π-electrons.[35] Excitation energies (E_{opt}) of all molecules are lowered in solvents showing the ease of electron excitations in solvent phase as compared to the gaseous phase *i.e.*, E_{opt} of **GY** and **2GY** is shifted from 4.72 and 4.60 eV to 4.68 and 4.51 eV.

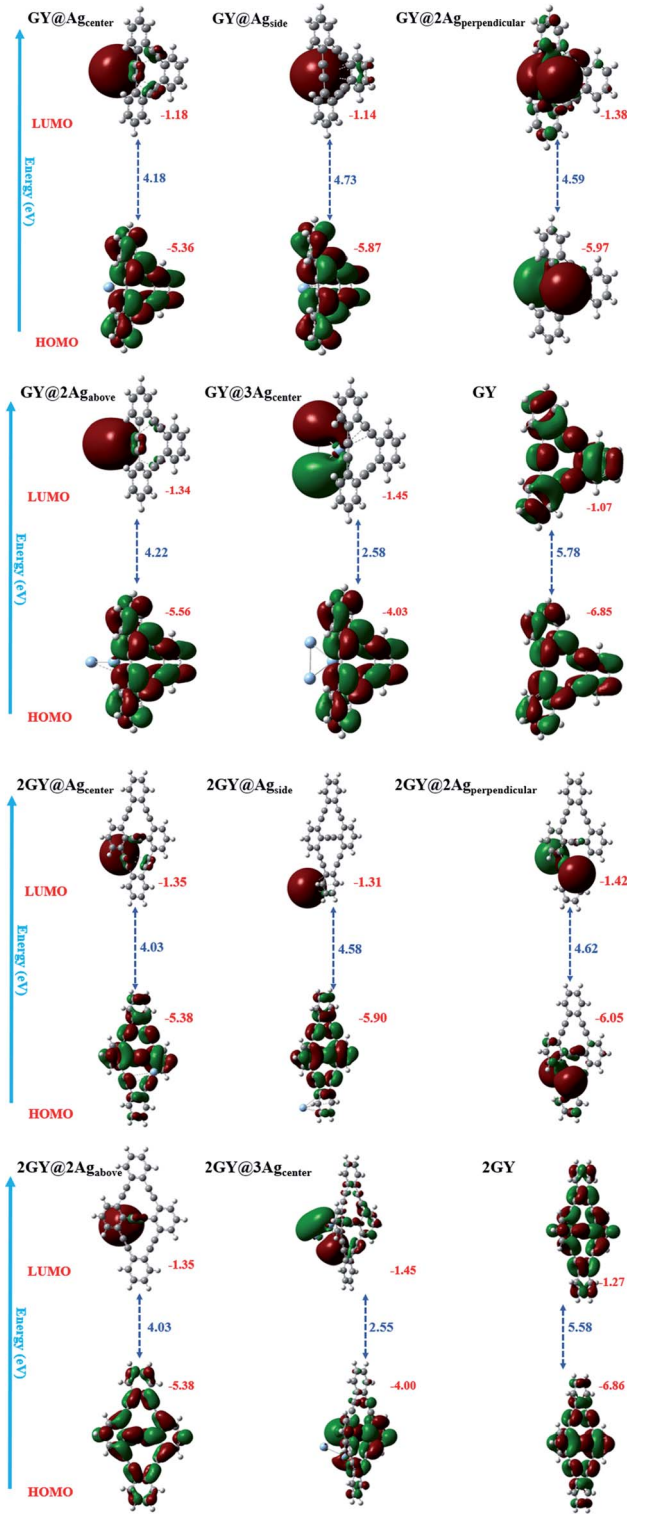

Fig. 9 FMO plots and band gaps (E_g) of all studied complexes along with pure surfaces.

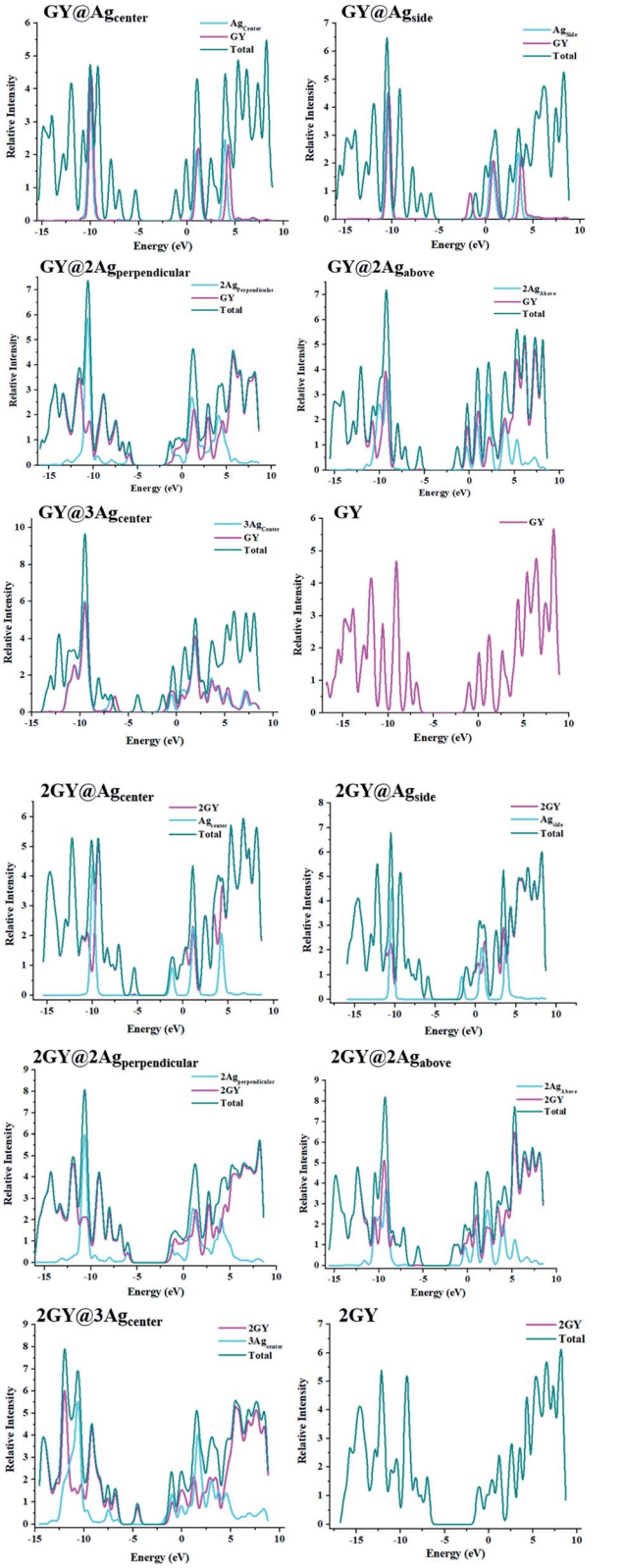

Fig. 10 DOS charts for molecules od model 1 and model 2.

Table 4 Surface and dopant role in developing the HOMO and LUMO of surface and all doped complexes

	HOMO = H		
Molecules	LUMO = L	GY	Dopant
GY	H	100	—
	L	100	—
GY@Ag$_{center}$	H	3.3	96.7
	L	100	0
GY@Ag$_{side}$	H	0.6	99.4
	L	99.7	0.3
GY@2Ag$_{perpendicular}$	H	47.2	52.8
	L	9.5	90.5
GY@2Ag$_{above}$	H	2.4	97.6
	L	99.7	0.3
GY@3Ag$_{center}$	H	0.6	99.4
	L	100	0
2GY	H	100	—
	L	100	—
2GY@Ag$_{center}$	H	1.8	98.2
	L	97.0	3.0
2GY@Ag$_{side}$	H	0.1	99.9
	L	99.3	0.7
2GY@2Ag$_{perpendicular}$	H	1.0	99.0
	L	98.3	1.7
2GY@2Ag$_{above}$	H	10.5	89.5
	L	47.6	52.4
2GY@3Ag$_{center}$	H	18.8	81.2
	L	82.7	17.3

Shifting of molecular transitions to higher percentage also signifies ease of electronic excitation from HOMO to LUMO energy levels. Graphical comparative study of absorption maximum of all molecules of models 1 and 2 in gaseous and solvent phase is revealed in Fig. 5. Similarly, Fig. 6 illustrates graphical comparison of E_{opt} in gaseous and solvent phases.

It has been noted that photophysical properties revealed by doped systems of model 2 are associated with higher $\lambda_{max}$and lower E_{opt} due to extended conjugation in two-unit cells of **GY**.

3.3 Frontier molecular orbitals (FMOs)

Analyzing FMOs of molecules is an essential tool used to determine charge mobility.[36] It is also relevant in explaining the charge transfer and distribution patterns in doped systems. Molecular systems having the highest occupied (HOMO) and lowest unoccupied (LUMO) energies have a substantial impact on electronic properties and absorption attributes.[37] HOMO has condensed population electronic charge while LUMO has only high energy charges similar to the valence band and conduction band of band theory, respectively.

Band gap (E_g) has been determined by following eqn (5).[38]

$$E_g = E_{LUMO} - E_{HOMO} \quad (5)$$

Here, E_{LUMO} and E_{HOMO} are LUMO and HOMO energies.

HOMO and LUMO energies together with their E_g are examined for both models 1 and 2 and their values are presented in Table 3. In pure **GY** and **2GY**, HOMO lie at −6.85 and −6.86 eV respectively while their LUMOs lie at 1.07 and 1.27 eV with a E_g of 5.78 and 5.58 respectively. Practically charge mobility is governed by the E_g. Lower E_g allows the charge to be excited and transported more efficiently across the pi-conjugated system. E_g and electrical conductivity are intrinsically linked. E_g of all doped systems is narrow when compared to **GY** and lies at 4.18, 4.73, 4.59, 4.22, and 2.58 eV for **GY@Ag$_{center}$**, **GY@Ag$_{side}$**, **GY@2Ag$_{perpendicular}$**, **GY@2Ag$_{above}$**,

Table 5 Computed dipole moment of all doped complexes of model 1 and model 2 in gaseous phase (μ_g), excited phase (μ_e) and transition electric dipole moment ($\Delta\mu$)

Molecules	μ_g (D)	μ_e (D)	$\Delta\mu$ (au)
GY	0.001	0.001	3.157
GY@Ag$_{center}$	1.455	1.218	0.940
GY@Ag$_{side}$	0.975	0.570	0.004
GY@2Ag$_{perpendicular}$	0.418	0.385	2.115
GY@2Ag$_{above}$	3.479	2.556	2.588
GY@3Ag$_{center}$	4.871	3.873	1.601
2GY	0.001	0.001	4.48
2GY@Ag$_{center}$	1.349	1.191	0.97
2GY@Ag$_{side}$	0.999	0.671	0.97
2GY@2Ag$_{perpendicular}$	0.136	0.509	2.13
2GY@2Ag$_{above}$	3.341	2.939	2.67
2GY@3Ag$_{center}$	3.628	6.998	1.69

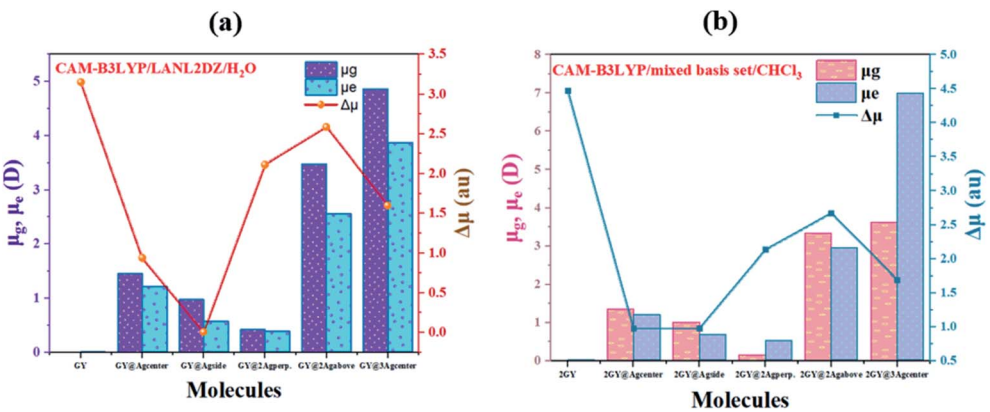

Fig. 11 Graphical representation of dipole moments at ground (μ_g), excited (μ_e) and transition electric dipole moment ($\Delta\mu$) of (a) **GY** and complexes **GY@Ag$_{center}$**–**GY@3Ag$_{center}$** and (b) **2GY** and complexes **2GY@Ag$_{center}$**–**2GY@3Ag$_{center}$**.

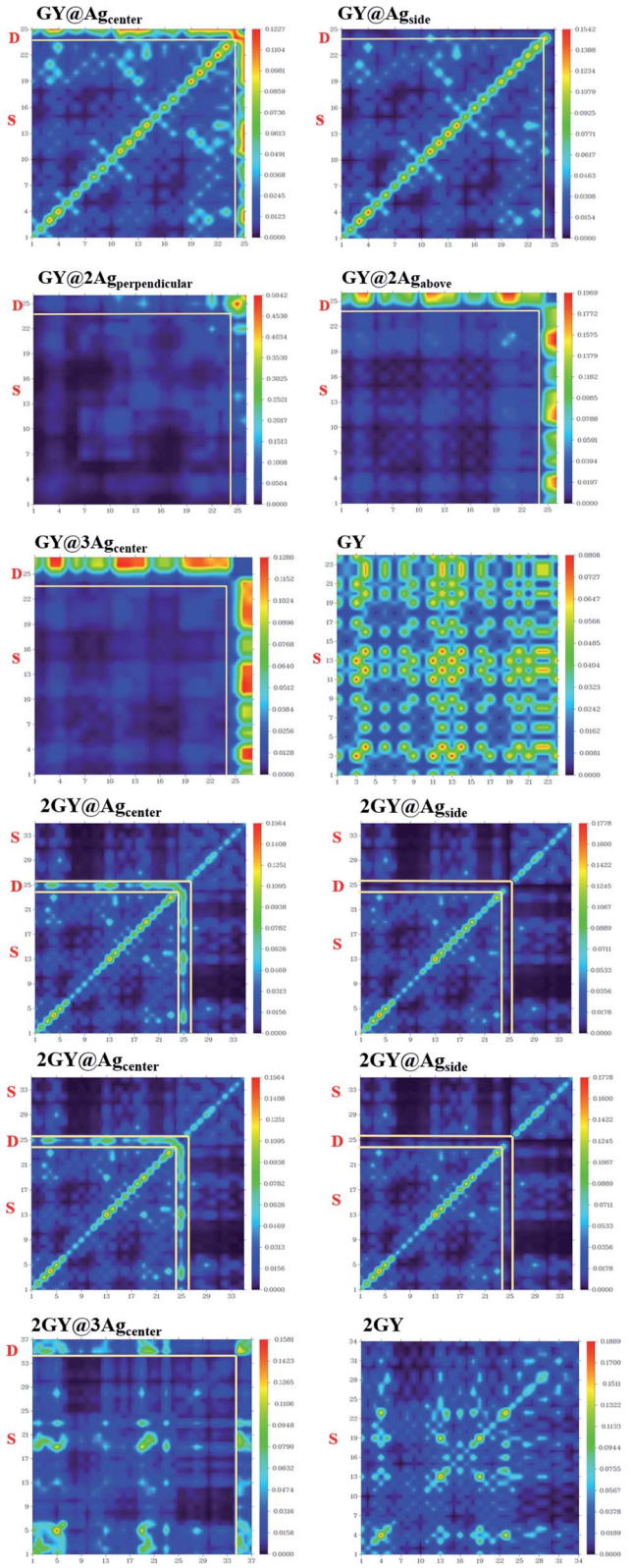

Fig. 12 TDM plots of pure surfaces and all molecular systems of model 1 and model 2. (a) GY and (GY@Ag$_{center}$–GY@3Ag$_{center}$) and (b) 2GY and (2GY@Agcenter–2GY@3Agcenter).

and **GY@3Ag$_{center}$** respectively. Narrow E_g in **GY@3Ag$_{center}$** validates enhanced conduction capacity. Due to low values E_g, all modeled doped systems (**GY@Ag$_{center}$**–**GY@3Ag$_{center}$**) are referred as polarizable, as well as efficient charge transfer complexes. Molecules of model 2 also indicated lower values of E_g as compared to their pure surface (**2GY**) and complexes of model 1 (**GY**–**GY@3Ag$_{center}$**). Lowest E_g is shown by **2GY@3Ag$_{center}$** of 2.55 eV. Values of HOMOs and LUMOs are pictured in Fig. 7.

Internal energy (E_{int}) refers to the stability of a molecule. Increase in E_{int} is associated with the increase in contact between dopant and surface, ultimately increasing the stability of the complex.[39] To study the thermodynamic stability of our doped complexes (**GY@Ag$_{center}$**–**GY@3Ag$_{center}$**) vertical ionization energy E_{VI} and E_{int} of complexes are determined computationally. From Table 3, it is inferred that values of E_{int} for **GY@Ag$_{center}$**, **GY@Ag$_{side}$**, **GY@2Ag$_{perpendicular}$**, **GY@2Ag$_{above}$**, and **GY@3Ag$_{center}$** are −1.69, −0.97, 14.69, −6.18, and −9.44 kcal mol^{-1} respectively for model 1 complexes. Model 2 molecular systems, on the other hand, are more stable and possess strong interaction between 2Ag dopant in perpendicular direction with **2GY**. Among all doped complexes, **2GY@2Ag$_{perpendicular}$** is the most stable as it possesses the highest E_{int}. Likewise, the highest E_{VI} is also revealed by **2GY@2Ag$_{perpendicular}$** verifying it is a stable complex among doped systems.

To acquire a better understanding of structural stability of complexes binding energy (E_b) is computed theoretically. E_b of pure **GY** and **2GY** surfaces as well doped systems (**GY@Ag$_{center}$**–**2GY@3Ag$_{center}$**) are calculated to explore the chemical stabilities using following eqn (6).[40,41]

$$E_b = E_g - E_{opt} \quad (6)$$

Here E_b is binding energy, E_g is band gap and E_{opt} is first excitation energy. Molecular systems possessing higher values of E_b are chemically stable and retain strong interaction between pure **GY** and dopants.[21] Among model 1 systems **GY@Ag$_{side}$** and **GY@2Ag$_{perpendicular}$** of newly doped systems explored higher values of E_b when compared to pure **GY**, confirming efficient

Table 6 Computed linear (α_O) and first hyperpolarizability (β_O) of surface as well as doped complexes

Molecules	α_O (au)	β_O (au)
GY	282	0.21
GY@Ag$_{center}$	326	1797
GY@Ag$_{side}$	333	1667
GY@2Ag$_{perpendicular}$	368	2188
GY@2Ag$_{above}$	371	2757
GY@3Ag$_{center}$	437	5049
2GY	416	0.06
2GY@Ag$_{center}$	460	1816
2GY@Ag$_{side}$	469	1828
2GY@2Ag$_{perpendicular}$	503	2449
2GY@2Ag$_{above}$	506	2964
2GY@3Ag$_{center}$	586	17 270

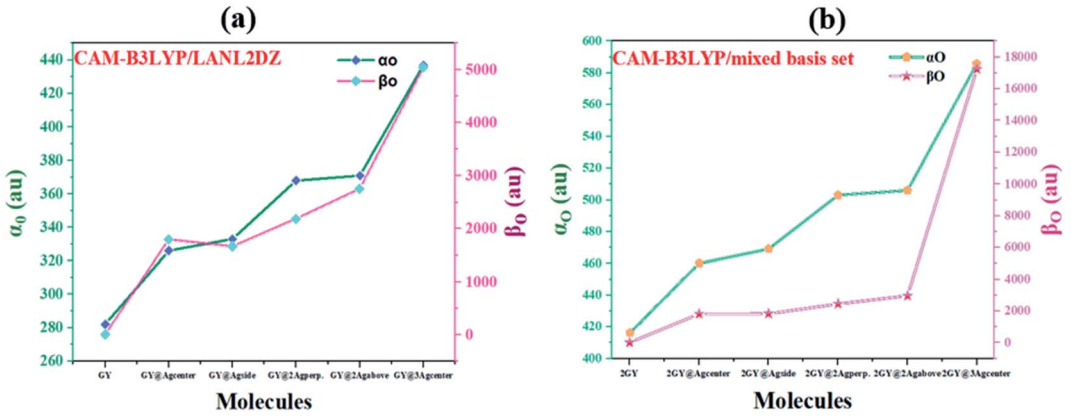

Fig. 13 Graphical representation of computed polarizabilities (a) GY and complexes $GY@Ag_{center}$–$GY@3Ag_{center}$ and (b) 2GY and complexes $2GY@Ag_{center}$–$2GY@3Ag_{center}$.

doping strategy on **GY** surface. Likewise, similar combinations of model 2 *i.e.*, $\mathbf{2GY@Ag_{side}}$ and $\mathbf{2GY@2Ag_{perpendicular}}$ showed higher E_b. While comparing the E_b of the two models, it was noticed that all of the molecules in model 2 showed a change in E_b towards a higher value. Graphical representation of E_b of all complexes is shown in Fig. 8.

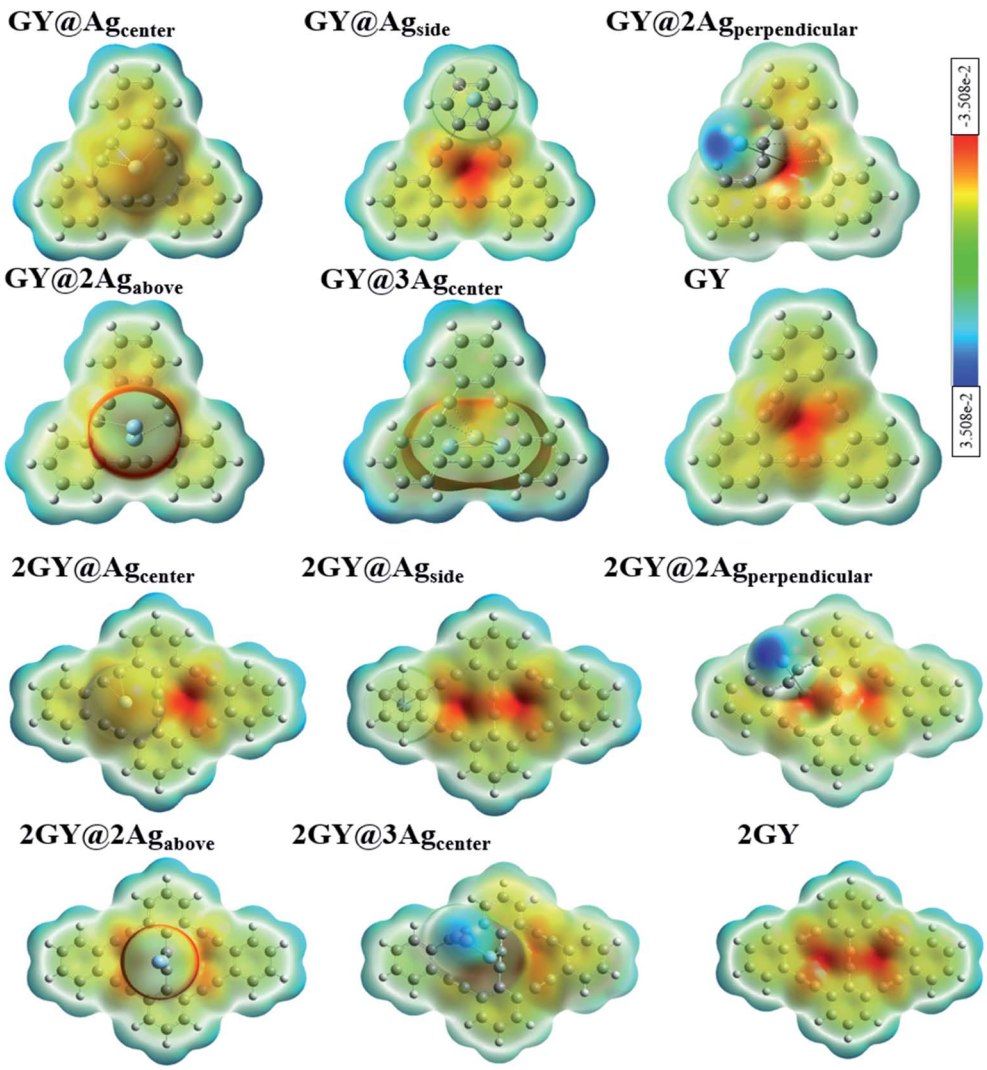

Fig. 14 ESP images of pure GY as well as $GY@Ag_{center}$–$GY@3Ag_{center}$ and 2GY as well as $2GY@Ag_{center}$–$2GY@3Ag_{center}$.

All analysed doped systems have their delocalization spread across the whole system.[42] In all complexes distribution pattern of energy orbitals is similar in a manner that HOMOs are concentrated over surfaces (**GY**) and (**2GY**) whereas LUMOs are condensed majorly on dopant and negligibly on surfaces.[42] FMO plots of pure **GY** and all studied molecules (**GY@Ag$_{center}$**–**2GY@3Ag$_{center}$**) along with their E_g are displayed in Fig. 9.

3.4 Density of states (DOS)

DOS is an analytical approach for analysing charge transport occupancy of states.[43] Mulliken charge distribution has supported FMO results. DOS research reveals how the fragmentation of the molecules raises the HOMO and LUMO molecular orbitals.[44] HOMO and LUMO energies can also be inferred *via* DOS approximations. DOS plots have been demonstrated to understand the role of the complexes and their fragments for the investigation of chemical bandgap. The DOS graphs of all researched molecules are evinced in Fig. 10. Table 4 summarizes the participation of various sections in formulating of molecular orbitals. In **GY** and **2GY**, both HOMO and LUMO are formed completely by the contribution of the surfaces. The influence of several sections in making of molecular orbitals in (**GY@Ag$_{center}$**–**GY@3Ag$_{center}$**) and (**2GY@Ag$_{center}$**–**2GY@3Ag$_{center}$**) is same. In these doped complexes, HOMO is acquired principally by the dopant and insignificantly by surfaces (**GY** and **2GY**) while in the formation of LUMO **GY** and **2GY** plays a substantial role.

3.5 Dipole moment (μ)

The dipole moment (μ) plays a key role in molecular packing and crystallinity.[45] The more the crystalline material is, the less likely it is for charge transfer states to behave abnormally.[46] Dipole

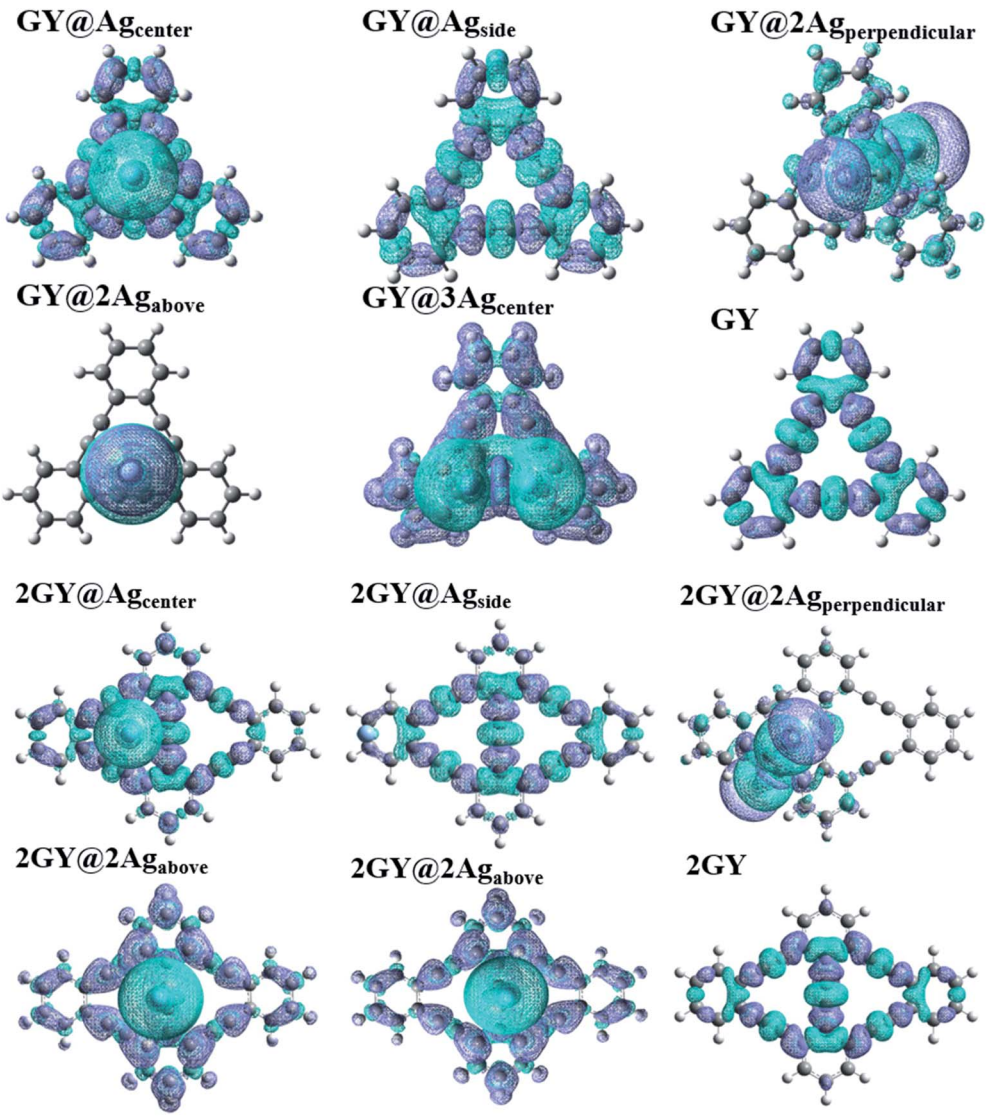

Fig. 15 EDDM images of pure **GY** as well as **GY@Ag$_{center}$**–**GY@3Ag$_{center}$** and **2GY** as well as **2GY@Ag$_{center}$**–**2GY@3Ag$_{center}$**.

moment in gaseous (μ_g), excited phase (μ_e) and transition electric dipole moment ($\Delta\mu$) is estimated using CAM-B3LYP/LANL2DZ functional for model 1 molecules while model 2 molecular systems are discussed using CAM-B3LYP functional with mixed basis set. Computed values of dipole moments are reviewed in Table 5. Findings showed that all our doped molecules (**GY@Ag$_{center}$**–**GY@3Ag$_{center}$**) and (**2GY@Ag$_{center}$**–**2GY@3Ag$_{center}$**) acquired more μ_g and μ_e than their respective surfaces (**GY** and **2GY**).

Pure **GY** and **2GY** reveal lower μ_g and μ_e of 0.001 and 0.001 D respectively due to symmetry in its structure. Among all molecules of model 1, **GY@3Ag$_{center}$** revealed maximum value of μ_g (4.871 D) and μ_e (3.873 D) possessing three Ag atom clusters which facilitate self-assembly and aid in multilayer fabrication. Increasing order of μ_e is **GY**< **GY@2Ag$_{perpendicular}$**< **GY@Ag$_{side}$**< **GY@Ag$_{center}$**< **GY@2Ag$_{above}$**< **GY@3Ag$_{center}$**. Same trend of increasing dipole moment is followed in the gaseous state. Hence, significant NLO properties can be achieved. Likewise, model 2 molecules also illustrated a significant shift towards high value in comparison with **2GY** and model 1 system. The impressive change in μ infers that complexes have arrayed themselves so as to limit recombination of charges. Dipole moments are graphically illustrated in Fig. 11.

3.6 Transition density matrix (TDM)

TDM refers to the matrix that dispenses information about charge transition locations and quantum geometry of doped molecules in excited state.[47,48] In TDM plots, the number of atoms is given on the *x*-axis and *y*-axis (left side) while on the right side of the *y*-axis coefficient of transition or electron density is displayed. Using the specified hybrid DFT functional, TDM analysis of pure **GY** and **2GY** and currently doped molecules (**GY@Ag$_{center}$**–**GY@3Ag$_{center}$**) and (**2GY@Ag$_{center}$**–**2GY@3Ag$_{center}$**) has been accomplished. Because of insignificant contributions in transitions, hydrogens atoms have been overlooked. Fig. 12 shows a visual representation of all molecules. **GY** and **2GY** are divided into one component while all other systems are sequestered into two fractions: surface and dopant.

In pure **GY** and **2GY**, charge distribution and coherency can be accomplished by valuable diagonal as well as off-diagonal charge transfer. In all designed doped materials, electronic distribution is concentrated on dopant portions. The bright spots on TDM are pointing to the atom number where the transition population was detected. The doped materials had exhibited enhanced charge transfer from surface to dopant. So, (**GY@Ag$_{center}$**–**GY@3Ag$_{center}$**) and (**2GY@Ag$_{center}$**–**2GY@3Ag$_{center}$**) exhibit marvellous charge separation capability when studied in contrast to pure **GY** and **2GY**, as a result, they can be used as unintentional aspirants for future NLO materials with improved characteristics.

3.7 NLO properties

The most persuasive parameter to quantify the NLO properties of pure **GY** and doped materials is linear polarizability (α_O) first hyperpolarizability (β_O).[49] Both α_O and β_O of all molecules of model 1 and 2 are evaluated computationally at their respective functionals and basis set, and outcomes are disclosed in Table 6. Values of α_O and β_O of all complexes (**GY@Ag$_{center}$**–**GY@3Ag$_{center}$**) are contrasted with pure **GY**. α_O of pure **GY**

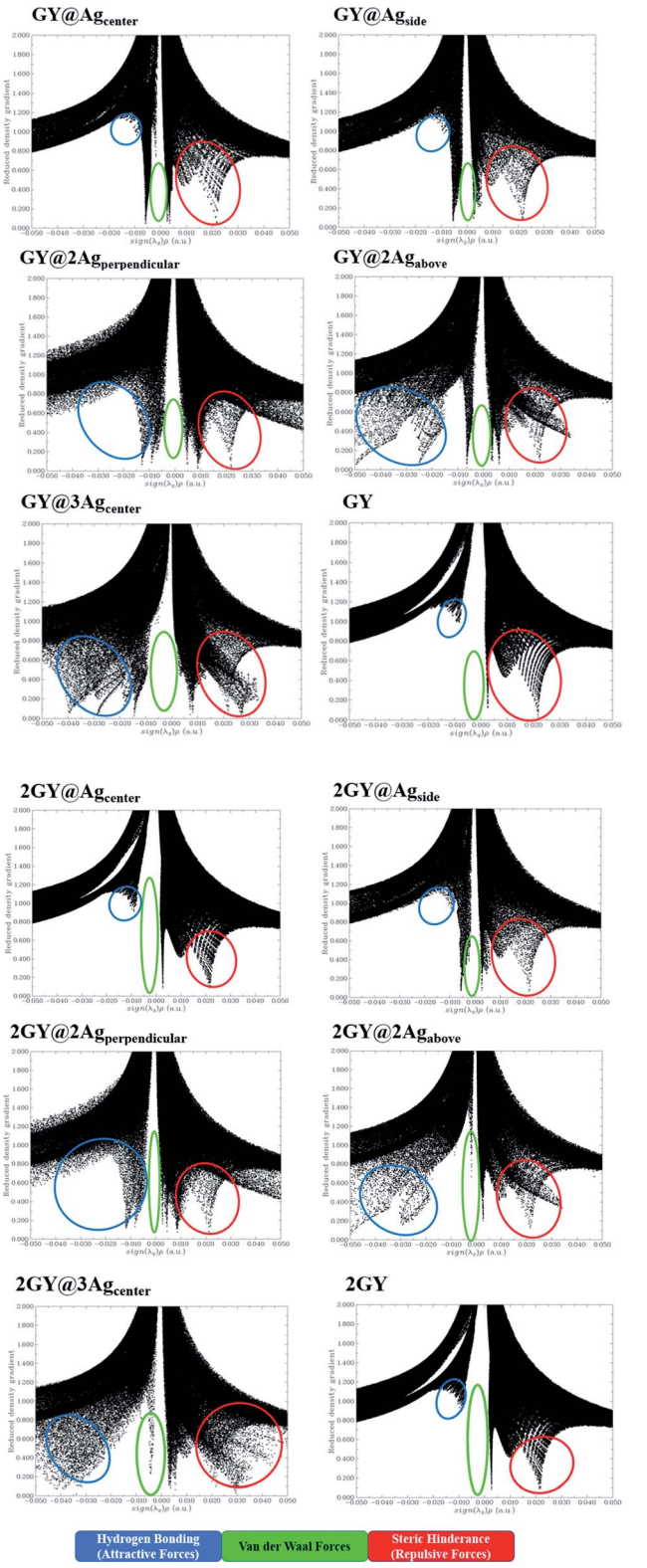

Fig. 16 NCI images for molecular complexes of model 1 as well as model 2.

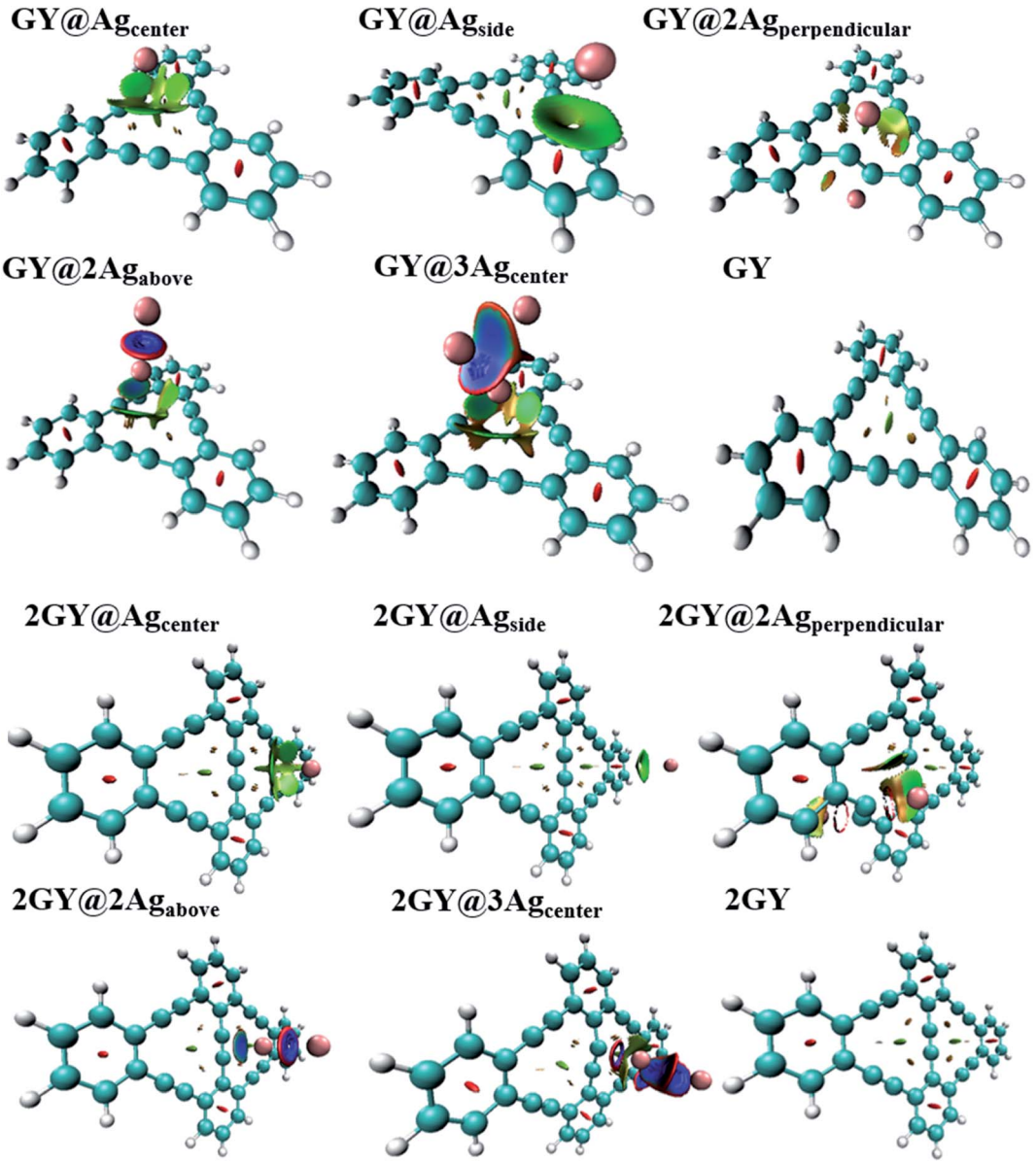

Fig. 17 Pictorial representation of 3D isosurface of all molecular complexes of model 1 as well as model 2.

surface lies at 282 au while doping of Ag clusters had prominently increased α_O in all doped complexes. α_O of **GY@Ag$_{center}$**, **GY@Ag$_{side}$**, **GY@2Ag$_{perpendicular}$**, **GY@2Ag$_{above}$**, and **GY@3Ag$_{center}$** are 326, 333, 368, 371, and 437 au respectively. 55% increase in linear polarizability α_O of **GY@3Ag$_{center}$** (437 au) is observed considering **GY** surface as a reference.

According to the literature, the NLO performance of a doped complex can be substantially intensified by the incorporation of surplus electrons. High energy HOMO levels are occupied by surplus electrons, leading to a decrease in E_g and elevation in β_O.[10] β_O of pure **GY** calculated computationally is 0.21 au. Pronounced shift in β_O of all doped complexes (**GY@Ag$_{center}$**–**GY@3Ag$_{center}$**) is observed. The β_O of all investigated complexes is decreasing as **GY@3Ag$_{center}$** (5049 au) > **GY@2Ag$_{above}$** (2757 au) > **GY@2Ag$_{perpendicular}$** (2188 au) > **GY@Ag$_{center}$** (1797 au) > **GY@Ag$_{side}$** (1667 au) > **GY** (0.21 au). Molecular systems of model 2 (**2GY@Ag$_{center}$**–**2GY@3Ag$_{center}$**) indicated sharp increase in α_O and β_O of complexes. **2GY@3Ag$_{center}$** acquired β_O of 17 270 au. The graphical representation of α_O and β_O is pictured in Fig. 13, representing β_O has increased several folds when studied in comparison with **GY**. Keeping in view the analysis of NLO properties, it is inferred that all our designed doped complexes specially complexes having two-unit cells of **GY** *i.e.*, (**2GY@Ag$_{center}$**–**2GY@3Ag$_{center}$**), will exhibit magnificent NLO responses.

3.8 Electron density and electrostatic potential (ESP) analysis

Electron density (ED) analysis grasps information regarding the reactivity of atoms and the presence of reactive sites for nucleophilic and electrophilic attack based on the distribution of the

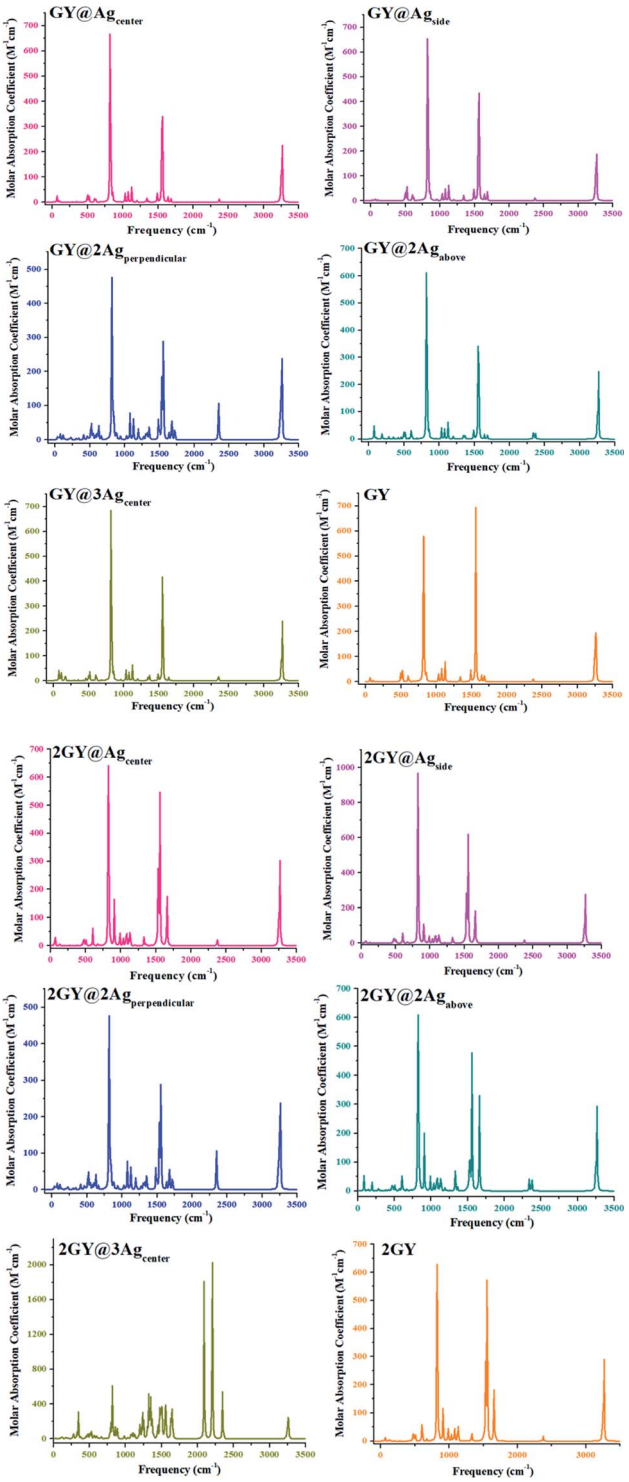

Fig. 18 IR plots of pure surfaces and all molecular systems of model 1 and model 2.

Milliken charge on the whole molecule.[50] ESP is also crucial in predicting the correlation among molecular structure, molecular interaction, as well as photophysical properties of molecules.[51] The electrophilic and nucleophilic regions of researched molecules are determined using ESP simulations conducted at optimal DFT functional. In ESP diagrams, red hue reflects the electrophilic, electron rich and negative ESP zone whereas the green hue signifies neutral zone, and the blue hue is concentrated on the nucleophilic, electrons deficient and positive ESP zone.[36]

ESP analysis of all doped complexes along with **GY** and **2GY** is done theoretically. Fig. 14 shows ESP diagrams of the pure surfaces along with freshly doped complexes. ESP diagrams of complexes of model 1 and model 2 demonstrate that the red color (negative potential) is concentrated on the acetylene region of the graphyne surface making it more electrophilic. The region where Ag dopant exists and backbone chain of surface in each molecular framework (**GY@Ag$_{center}$–GY@3Ag$_{center}$**) and (**2GY@Ag$_{center}$–2GY@3Ag$_{center}$**), possess blue color (positive potential) and behave as a nucleophile.

3.9 Electron density distribution matrix (EDDM)

To comprehend the charge transfer capacity, EDDM evaluations were also executed in which molecular orbitals of excited state are subtracted from ground state.[52] EDDM of all doped complexes (**GY@Ag$_{center}$–GY@3Ag$_{center}$**) along with **GY** is evaluated computationally at CAM-B3LYP/LANL2DZ functional while analysis of (**2GY@Ag$_{center}$–2GY@3Ag$_{center}$**) is done at CAMB3LYP/mixed basis set. EDDM graphs show the reorganization of electrons in pure surfaces and doped complexes. Fig. 15 shows the net charge density of subtracted complexes. Sea-green color in EDDM diagrams reveals a positive value of charge density while purple color illustrates the negative value and reduced electron density upon excitation. Charge distribution pattern in **GY**, **2GY**, **GY@Ag$_{center}$**, **2GY@Ag$_{center}$**, **GY@Ag$_{side}$**, **2GY@Ag$_{side}$**, **2GY@2Ag$_{above}$**, and **GY@3Ag$_{center}$**, **2GY@3Ag$_{center}$**, is analogous, in such a way that charge density is distributed evenly over the entire system. But in **GY@2Ag$_{perpendicular}$**, **2GY@2Ag$_{perpendicular}$**, and **GY@2Ag$_{above}$** charge distribution is mainly concentrated on dopant units.

3.10 Non-covalent interaction (NCI) analysis

The NCI assessment gives valuable information regarding a molecule's non-covalent interactions.[53] NCI plot can distinguish between the molecular areas with weak interactions and those with strong directional attractions associated with localised atom–atom linkages.[54] Fig. 16 depicts the scatter graphs drawn between the reduced density gradient and the electron density (r), oriented by the sign of λ_2.[55] NCI analysis appears to be a superior alternative for using data about hydrogen bonding, van der Waals forces, and steric hindrance inside a system to improve information on the molecular stability in small or large molecules.[55] The scatter graphs are created with Multiwfn software. The (λ_2) ρ values can be used to predict the nature of interaction: if (λ_2) $\rho > 0$ then the interaction is repulsive, and if (λ_2) $\rho < 0$ then the interaction is attractive that is also highlighted by color-filled 3D isosurface of complexes and graphyne, shown in Fig. 16. The NCI graphs of all doped systems along with surfaces (**GY** and **2GY**) show that strong attractive forces exist between the complex molecules that is advantageous for propitious NLO materials. The H-bond

Table 7 Computed IR frequencies of pure surface as well as all doped complexes

Molecules	Frequency (cm^{-1})	Vibrations	Molecules	Frequency (cm^{-1})	Vibrations
GY	64	Wagging	**2GY**	75	Wagging
	824	Twisting		822	Twisting
	1561	Scissoring		1557	Scissoring
	3266	Symmetrical stretching		3267	Symmetrical stretching
GY@Ag$_{center}$	66	Wagging	**2GY@Ag$_{center}$**	64	Wagging
	824	Twisting		825	Twisting
	1560	Scissoring		1557	Scissoring
	3266	Symmetrical stretching		3267	Symmetrical stretching
GY@Ag$_{side}$	64	Wagging	**2GY@Ag$_{side}$**	76	Wagging
	823	Twisting		828	Twisting
	1561	Scissoring		1557	Scissoring
	3267	Symmetrical stretching		3255	Symmetrical stretching
GY@2Ag$_{perpendicular}$	74	Wagging	**2GY@2Ag$_{perpendicular}$**	74	Wagging
	822	Twisting		822	Twisting
	1535	Scissoring		1535	Scissoring
	2348	Asymmetrical stretching		2348	Asymmetrical stretching
	3264	Symmetrical stretching		3264	Symmetrical stretching
GY@2Ag$_{above}$	77	Wagging	**2GY@2Ag$_{above}$**	96	Wagging
	823	Twisting		825	Twisting
	1561	Scissoring		1553	Scissoring
	3268	Symmetrical stretching		3266	Symmetrical stretching
GY@3Ag$_{center}$	80	Scissoring	**2GY@3Ag$_{center}$**	84	Scissoring
	823	Twisting		823	Twisting
	1558	Scissoring		2204	Scissoring
	3268	Symmetrical stretching		3264	Symmetrical stretching

(attractive) is shown by the blue tone, the van der Waals interactions are indicated by the green hue, and the steric effect is indicated by the red region (repulsive) (Fig. 17).

3.11 Infrared (IR) analysis

Infrared (IR) spectrum characteristics of pure graphyne and doped complexes are researched to analyze how they change with doping. Fig. 18 depicts the IR spectrum. In all IR spectra, frequencies around 64 to 77 cm^{-1} are due to wagging vibrations except for **GY@3Ag$_{center}$** and **2GY@3Ag$_{center}$** where 80 cm^{-1} frequency is for scissoring vibrations. Vibrational frequencies at around 800 cm^{-1}, 1550 cm^{-1}, and 3200 cm^{-1} in all systems are related to twisting, scissoring, and symmetrical stretching vibrations. Detailed study of vibrational frequencies of all studied molecules is illustrated in Table 7.

3.12 Electrical conductivity (σ)

Most crucial aspect in determining the electrical conductivity (σ) of doped complexes for NLO properties is E_g. After adsorbing the silver (Ag) clusters on the surface (**GY** and **2GY**), these unique complexes (**GY@Ag$_{center}$–GY@3Ag$_{center}$**) and (**2GY@Ag$_{center}$–2GY@3Ag$_{center}$**) become more semiconductor-like owing to their narrow E_g. Therefore, it is envisaged that the σ is increased as compared to pure surface and can be determined using eqn (6).[56]

$$\sigma\alpha \exp\left(\frac{-E_g}{2kT}\right) \quad (7)$$

Here, σ is electrical conductivity, E_g is the band gap, k is Boltzmann constant and T is the temperature in kelvin. From the equation, it is inferred that the doped complexes possessing lower E_g will have higher σ because it is exponentially correlated to E_g.[57] In our investigation of model 1 systems, E_g of all newly designed doped complexes has smaller values (in the range of 2.58 to 4.73 eV) in comparison with pure **GY** (5.78 eV) as indicated in Table 3 leading to the significant increase in electrical conductivities of doped complexes (**GY@Ag$_{center}$–GY@3Ag$_{center}$**). Likewise, all molecular systems (**2GY@Ag$_{center}$–2GY@3Ag$_{center}$**) are accompanied by relatively lower E_g and higher electrical conductivity (σ). Electrical conductivity of complexes lies in the order of **2GY@3Ag$_{center}$** > **2GY@Ag$_{center}$** = **2GY@2Ag$_{above}$** >**2GY@Ag$_{side}$** >**2GY@2Ag$_{perpendicular}$** > **2GY**. An increase in σ has resulted from strong dopant–surface interaction and efficient $n \rightarrow \sigma^*$ charge transfer. Thus, our designed Ag cluster doped complexes on the **2GY** surface may behave as unique sensing materials.

4. Conclusion

The current study relies on the comprehensive analysis of Ag cluster doped with graphyne surface in two distinct ways. In model 1, one-unit cell graphyne (**GY**) doped with variable Ag clusters produced complexes namely **GY@Ag$_{center}$**, **GY@Ag$_{side}$**, **GY@2Ag$_{perpendicular}$**, **GY@2Ag$_{above}$**, **GY@3Ag$_{center}$**, and employ CAM-B3LYP/LANL2DZ functional to explore the NLO properties. While in model 2, two-unit cell graphyne (**2GY**) doped with Ag are designed namely **2GY@Ag$_{center}$**, **2GY@Ag$_{side}$**, **2GY@2Ag$_{perpendicular}$**, **2GY@2Ag$_{above}$**, **2GY@3Ag$_{center}$** and their NLO properties are studied at CAM-B3LYP/mixed basis set. To study charge distribution FMOs, DOS, EDDM, TDM, and ESP

analysis were directed. Using E_{VI} and E_{int}, the thermodynamic stability of complexes has been explored. The simulated outcomes of all complexes lie in the range of efficient NLO material such as red-shifted λ_{max}, ameliorated α_O and β_O, narrowed E_g and lowered E_{opt} of all doped complexes in comparison with pure **GY** and **2GY**. Among molecular complexes of model 1; highest λ_{max} is exhibited by **GY@3Ag$_{center}$** (536 nm) with the lowest E_{opt} of 2.31 eV among all molecular systems. The newly doped systems (**GY@Ag$_{center}$–GY@3Ag$_{center}$**) are enriched with a higher dipole moment μ_e (0.385–3.873 D) in H_2O than **GY** (0.001 D). Likewise, **2GY@3Ag$_{center}$** has highest λ_{max} of 548 nm, lowest E_{opt} of 2.31 eV and much narrower E_g of 2.55 eV in model 2 complexes (**2GY@Ag$_{center}$–2GY@3Ag$_{center}$**). Infrared (IR) and NCI analysis are performed to study the types of vibrations associated and nature of interaction. Higher values of electrical conductivities of all complexes resulted from strong dopant–surface interaction and efficient n → σ* charge transfer. All computationally computed parameters advocate the potential of using all doped complexes of model 1 as well as model 2 in integrated NLO devices and open new routes for designing highly efficient NLO materials. Moreover, more virtuous and upstanding outcomes have been revealed by complexes in which graphyne surface was comprised of two-unit cell. To sum up, the current research yields deep insight into tuneable NLO characteristics of Ag doped on graphyne surface.

Author contributions

Saba Zahid: major contribution, the acquisition, drafting, analysis, writing original paper, working and interpretation of data.

Alvina Rasool: the acquisition, drafting, analysis, working, and interpretation of data.

Ali Raza Ayub: the acquisition, drafting, analysis, working, and interpretation of data.

Khurshid Ayub: the acquisition, drafting, analysis, working, and interpretation of data.

Javed Iqbal*: substantial contribution to research design, the acquisition, analysis, and interpretation of data, and approval of the submitted and final version. M. S. Al-Buriahi: the acquisition, drafting, analysis, working, and interpretation of data. Norah Alwadai: the acquisition, drafting, analysis, working, and interpretation of data. H. H. Somaily: the acquisition, drafting, analysis, working, and interpretation of data.

Conflicts of interest

There are no declared conflicts.

Acknowledgements

The authors thank the Punjab Bio-energy Institute (PBI), University of Agriculture (UAF), Faisalabad 38000, Pakistan, for financial and technical support. The authors express their gratitude to Princess Nourah bint Abdulrahman University Researchers Supporting Project (Grant No. PNURSP2022R11), Princess Nourah bint Abdulrahman University, Riyadh, Saudi Arabia. This work was supported by King Khalid University through a grant (RCAMS/KKU/G001/21) under the Research Center for Advanced Materials Science (RCAMS) at King Khalid University, Saudi Arabia.

References

1 A. Ahsin and K. Ayub, *Optik*, 2021, **227**, 166037.
2 O. Mhibik, S. Forget, D. Ott, G. Venus, I. Divliansky, L. Glebov and S. Chénais, *Light: Sci. Appl.*, 2016, **5**, e16026.
3 C. J. Brabec, *Sol. Energy Mater. Sol. Cells*, 2004, **83**, 273–292.
4 H. Hasegawa and T. Sato, *Electrochim. Acta*, 2005, **50**, 3015–3027.
5 C. Cheng, C. Zhu, B. Huang, H. Zhang, H. Zhang, R. Chen, W. Pei, Q. Chen and H. Chen, *Adv. Mater. Technol.*, 2019, **4**, 1800729.
6 J. M. Hales, M. Cozzuol, T. E. Screen, H. L. Anderson and J. W. Perry, *Opt Express*, 2009, **17**, 18478–18488.
7 S. Achelle, C. Baudequin and N. Plé, *Dyes Pigm.*, 2013, **98**, 575–600.
8 S. S. Varghese, S. Lonkar, K. Singh, S. Swaminathan and A. Abdala, *Sens. Actuators, B*, 2015, **218**, 160–183.
9 A. Karakas, A. Elmali and H. Unver, *Spectrochim. Acta, Part A*, 2007, **68**, 567–572.
10 R. Baloach, K. Ayub, T. Mahmood, A. Asif, S. Tabassum and M. A. Gilani, *J. Inorg. Organomet. Polym. Mater.*, 2021, **31**, 3062–3076.
11 M. Ishaq, R. A. Shehzad, M. Yaseen, S. Iqbal, K. Ayub and J. Iqbal, *J. Mol. Model.*, 2021, **27**, 1–11.
12 S. Muhammad, M. R. S. A. Janjua and Z. Su, *J. Phys. Chem. C*, 2009, **113**, 12551–12557.
13 R. A. Shehzad, S. Muhammad, J. Iqbal, A. G. Al-Sehemi, M. Yaseen, Z. Aloui and M. Khalid, *J. Mol. Model.*, 2021, **27**, 1–10.
14 A. U. Khan, S. Muhammad, R. A. Khera, R. A. Shehzad, K. Ayub and J. Iqbal, *Optik*, 2021, **231**, 166464.
15 A. Irfan, M. Pannipara, A. G. Al-Sehemi, M. W. Mumtaz, M. A. Assiri, A. R. Chaudhry and S. Muhammad, *Z. Phys. Chem. (Muenchen, Ger.)*, 2019, **233**, 1625–1644.
16 D. Xiao, F. A. Bulat, W. Yang and D. N. Beratan, *Nano Lett.*, 2008, **8**, 2814–2818.
17 L. Zhu, K. Xue and J. Hou, *J. Mol. Model.*, 2019, **25**, 1–10.
18 M. J. Lee, M. Piao, M.-Y. Jeong, S. H. Lee, K. M. Kang, S.-J. Jeon, T. G. Lim and B. R. Cho, *J. Mater. Chem.*, 2003, **13**, 1030–1037.
19 Y.-D. Song and Q.-T. Wang, *Optik*, 2020, **220**, 164947.
20 R. Baughman, H. Eckhardt and M. Kertesz, *J. Chem. Phys.*, 1987, **87**, 6687–6699.
21 X. Li and S. Li, *J. Mater. Chem. C*, 2019, **7**, 1630–1640.
22 M. Zhang, X. Wang, H. Sun, J. Yu, N. Wang, Y. Long and C. Huang, *2D Materials*, 2018, **5**, 035039.
23 A. Bhaskar, R. Guda, M. M. Haley and T. Goodson III, *J. Am. Chem. Soc.*, 2006, **128**, 13972–13973.
24 K. Srinivasu and S. K. Ghosh, *J. Phys. Chem. C*, 2012, **116**, 5951–5956.
25 H. Zhang, X. Zhao, M. Zhang, Y. Luo, G. Li and M. Zhao, *J. Phys. D: Appl. Phys.*, 2013, **46**, 495307.

26 M. Frisch, G. Trucks, H. Schlegel, G. Scuseria, M. Robb, J. Cheeseman, G. Scalmani, V. Barone, B. Mennucci and G. Petersson, *Google Scholar There is no corresponding record for this reference*, 2015.
27 T. Yanai, D. P. Tew and N. C. Handy, *Chem. Phys. Lett.*, 2004, **393**, 51–57.
28 A. Klamt, C. Moya and J. Palomar, *J. Chem. Theory Comput.*, 2015, **11**, 4220–4225.
29 S. Gorelsky, *A Library for Package-Independent Computational Chemistry Algorithms*, University of Ottawa, Ottawa, Canada, 2010.
30 A. S. Rad and K. Ayub, *J. Alloys Compd.*, 2016, **672**, 161–169.
31 R. A. Shehzad, J. Iqbal, K. Ayub, F. Nawaz, S. Muhammad, A. R. Ayub and S. Iqbal, *Optik*, 2021, **226**, 165923.
32 N. M. O'boyle, A. L. Tenderholt and K. M. Langner, *J. Comput. Chem.*, 2008, **29**, 839–845.
33 T. Lu and F. Chen, *J. Comput. Chem.*, 2012, **33**, 580–592.
34 M. R. S. A. Janjua, C.-G. Liu, W. Guan, J. Zhuang, S. Muhammad, L.-K. Yan and Z.-M. Su, *J. Phys. Chem. A*, 2009, **113**, 3576–3587.
35 M. R. S. A. Janjua, Z. H. Yamani, S. Jamil, A. Mahmood, I. Ahmad, M. Haroon, M. H. Tahir, Z. Yang and S. Pan, *Aust. J. Chem.*, 2015, **69**, 467–472.
36 S. Zahid, A. Rasool, M. Ans, M. Yaseen and J. Iqbal, *Energy Fuels*, 2021, **35**, 15018–15032.
37 A. Rasool, S. Zahid, R. A. Shehzad, M. S. Akhter and J. Iqbal, *Comput. Theor. Chem.*, 2021, **1203**, 113359.
38 A. U. Khan, R. A. Khera, N. Anjum, R. A. Shehzad, S. Iqbal, K. Ayub and J. Iqbal, *RSC Adv.*, 2021, **11**, 7779–7789.
39 F. Ullah, N. Kosar, K. Ayub, M. A. Gilani and T. Mahmood, *New J. Chem.*, 2019, **43**, 5727–5736.
40 S. Zahid, A. Rasool, M. Ans, M. Salim Akhter, J. Iqbal, M. S. Al-Buriahi, S. Alomairy and Z. A. Alrowaili, *Sol. Energy*, 2022, **231**, 793–808.
41 A. Rasool, S. Zahid, M. Ans, J. Iqbal, M. Adnan, E.-S. M. Sherif and M. S. Al-Buriahi, *Opt. Mater.*, 2022, **123**, 111907.
42 R. Habibpour and R. Vaziri, *Int. J. Nano Dimens.*, 2016, **7**, 208–224.
43 G. Landi, H. C. Neitzert, C. Barone, C. Mauro, F. Lang, S. Albrecht, B. Rech and S. Pagano, *Adv. Sci.*, 2017, **4**, 1700183.
44 F. Ullah, N. Kosar, M. N. Arshad, M. A. Gilani, K. Ayub and T. Mahmood, *Opt Laser. Technol.*, 2020, **122**, 105855.
45 H. H. Cho, S. Kim, T. Kim, V. G. Sree, S. H. Jin, F. S. Kim and B. J. Kim, *Adv. Energy Mater.*, 2018, **8**, 1701436.
46 F. Manzoor, J. Iqbal, Z. Zara, B. Eliasson, M. S. Mahr and K. Ayub, *ChemistrySelect*, 2018, **3**, 1593–1601.
47 S. Zahid, A. Rasool, R. A. Shehzad, I. A. Bhatti and J. Iqbal, *J. Mol. Model.*, 2021, **27**, 1–14.
48 A. Rasool, S. Zahid, M. Ans, S. Muhammad, K. Ayub and J. Iqbal, *ACS Omega*, 2021, **7**, 844–862.
49 M. U. Khan, M. Ibrahim, M. Khalid, S. Jamil, A. A. Al-Saadi and M. R. S. A. Janjua, *Chem. Phys. Lett.*, 2019, **719**, 59–66.
50 S. Iyasamy, K. Varadharajan and S. Sivagnanam, *Z. Phys. Chem. (Muenchen, Ger.)*, 2016, **230**, 1681–1710.
51 M. Drissi, N. Benhalima, Y. Megrouss, R. Rachida, A. Chouaih and F. Hamzaoui, *Molecules*, 2015, **20**, 4042–4054.
52 R. Kiran, R. A. Khera, A. U. Khan, A. Ayoub, N. Iqbal, K. Ayub and J. Iqbal, *J. Mol. Struct.*, 2021, **1236**, 130348.
53 I. Munir, M. Perveen, S. Nazir, R. A. Khera, A. R. Ayub, K. Ayub and J. Iqbal, *J. Mol. Liq.*, 2021, **336**, 116327.
54 M. D. Mohammadi, 2021.
55 M. D. Mohammadi and H. Y. Abdullah, *J. Mol. Model.*, 2020, **26**, 1–15.
56 X. Li and J. Lu, *Phys. Chem. Chem. Phys.*, 2019, **21**, 13165–13175.
57 L. Ma, J.-M. Zhang, K.-W. Xu and V. Ji, *Appl. Surf. Sci.*, 2015, **343**, 121–127.